Filling spherical surfaces by mixed triangle and square tiles

Han Xie [1], Yao Li [2,*] and Jeff Z. Y. Chen [1,†]

[1]*Department of Physics and Astronomy, University of Waterloo, Ontario, Canada N2L 3G1*

[2]*School of Physics and Key Laboratory of Functional Polymer Materials of Ministry of Education, Nankai University, and Collaborative Innovation Center of Chemical Science and Engineering, Tianjin 300071, China*

(Received 20 November 2024; accepted 10 March 2025; published 10 April 2025)

We present four classes of highly symmetric defect patterns on a spherical surface tiled with triangular and square tiles. These patterns accommodate both stretched triangular and square lattices and are analyzed in terms of their symmetries. Both spherical and corresponding polyhedron views are considered, with emphasis on three-dimensional point-group symmetries. In addition to the original patterns, alternative defect configurations are explored, including those generated by the kaleidoscopic operation, originally suggested by Caspar and Klug for triangular tiling, as well as the cut-and-rotate operation applied through a great circle on the sphere. While these alternatives can lower the space-group symmetries, they provide a broader understanding of the system's possible configurations. For a fixed square surface area fraction, we also examine a scenario that identifies the likely ground state among the four primary classes and their alternatives.

DOI: 10.1103/PhysRevE.111.045408

I. INTRODUCTION

Placing triangular tiles to fill the surface of a sphere, what high-symmetry patterns can they form? This is a classical question studied by Caspar and Klug [1]. Unlike regularly tiled lattices in a flat space, which can yield translational and rotational symmetries, triangular tiling on a spherical surface necessitates lattice disclinations, dictated by the nature of the curved two-dimensional surface [2]. Typical high-symmetry patterns observed in this example, resulting from the 12 point defects of fivefold symmetry along with the filling lattice textures, include the icosahedron, dodecahedron, and their kaleidoscopic alternatives [1].

The study of lattice construction on spherical surfaces has its roots in investigating the structural organization of viruses. Early investigations into how protein blocks self-assemble on spherical surfaces were advanced by techniques such as cryo-electron microscopy and x-ray crystallography [3]. In the 1950s, Crick and Watson [4] proposed that spherical viruses were composed of 60 identical triangular subunits, exhibiting icosahedral symmetry. However, experimental findings later revealed that many viruses have more than 60 subunits [5]. Caspar and Klug [1] developed a theoretical method to arrange a large number of triangular subunits on spherical surfaces, effectively addressing the issue of spherical virus structure. The defect pattern follows the icosahedron symmetry, as noted by Goldberg who studied the geometry of polyhedra with all triangular faces [6]. Their methods closely resembled the geodesic dome structure proposed by Buckminster Fuller in the late 1940s, a concept that also inspired the discovery of fullerene [7]. Building on this research, various icosahedral virus structures, consisting of protein blocks in different shapes, have been revealed [8,9]. By utilizing protein blocks of three- and sixfold symmetries, which can be nicely tiled in a triangular lattice cell, icosahedral protein cages and capsules are designed and manufactured [10,11] for industrial, pharmaceutical, and scientific uses. The construction method for spherical triangular lattices also finds applications in soft materials [12,13] and crystalline solids [14,15].

What happens when the spherical surface is covered by square lattices or liquid crystals made of molecules having tetratic symmetry? Experimentally, stabilizing square lattices on a spherical surface is more challenging because thin-layer molecules tend to form triangular lattices in real systems. Variations of tiling that use tetratically shaped particles to fit the spherical surface while maintaining the local fourfold symmetry have been explored in recent years, for example, with square-shaped protein blocks [16], rounded cube particles on emulsion faces [17], or tetratic liquid-crystal molecules [18,19]. Analytic theories that explore the possible symmetry patterns of related systems can also be found for liquid crystals [20], and square crystalline and liquid crystals [19]. Direct molecular-level computer simulations that yield local square lattices with a limited number of particles are now available [15,21,22]. To answer the question of what defect patterns can be observed in square tilings on the spherical surface, the cube and anticube symmetries suggested in Refs. [18,19] for arranging tetratic molecules are further explored in Sec. II through a symmetry analysis which also generates additional alternatives.

Then, what symmetry patterns can one observe when mixed triangular and square tiles are used to cover the spherical surface? This question is inspired by both experimental and theoretical developments in recent years. Investigations have shown that structures formed by mixing protein block

*Contact author: liyao@nankai.edu.cn

†Contact author: jeffchen@uwaterloo.ca

shapes with three- and fourfold local symmetries on spherical surfaces can exhibit octahedral and tetrahedral symmetries. These symmetries differ from the icosahedral symmetry typically observed on the surfaces of other protein complexes [23–25]. When highly packed on a flat surface, isotropic molecules can form triangular and square lattice domains, which coexist under the right physical conditions, as has been recently observed in both experiments [26–30] and computer simulations [22,31,32]. On spherical surfaces and under the correct overall molecular density, these molecules self-assemble into defect domains composed of triangular and square tiles, each domain carrying characteristic winding numbers, as reported by computer simulations [33,34]. Theoretically, except for the structures found through the Caspar-Klug construction method for triangular tiles on a spherical surface, there have been no definitive answers to this question in the literature so far.

In this paper, we develop a general theory to construct mixed triangular and square lattices on spherical surfaces, where the square lattice area occupies a fraction f of the surface and the triangular lattice area the remainder. A large number of tiles is assumed here, and the coarse-grained continuum limit is examined. Two issues, symmetry and energetics, are addressed separately in Secs. II and III. For consistency, the symmetry problems of tiling the spherical surface with only triangular tiles ($f = 0$) and only square tiles ($f = 1$) are first reviewed in Secs. II A and II B, respectively. In the case of a fixed, nontrivial value of f, we enumerate all possible high-symmetry patterns formed by defect points and lattice texture grains. Four classes of patterns, cubic (O_h), octahedral (O_h), tetrahedral (T_d), and trihosohedral (D_{3h}) symmetries, are selected, listed, and analyzed in Sec. II C. With one or two symmetry operations broken, kaleidoscopic alternatives, originally introduced by Caspar and Klug, are also considered in Sec. II E [1], forming face-rotation (FR) alternatives of the patterns. Another possibility, known as the cut-and-rotate (CR) operation [35,36], is additionally introduced and considered for these symmetric patterns in Sec. II F, forming the CR alternatives. Both alternatives preserve the lattice grains and result in lower spatial symmetries than the original O_h, T_d, D_{3h} rotational groups.

The second issue is to consider which of the listed patterns in Sec. II is energetically more favorable in a real molecular system. This is a subtle question that depends on the microscopic nature of the interaction energy, the formed material phases (liquid, liquid crystal, or crystal) and the size of the final system; there is no general answer. Bowick, Nelson, and Travesset (BNT) developed a coarse-grained interaction energy between the defect points, induced by the elastic stretching of an otherwise flat lattice pattern on a curved spherical surface [37]. As an example, based on the assumption of a continuum limit that ignores molecular details, the BNT interaction energy is used in Sec. III for comparison between the selected symmetries in Sec. II for a fixed f. Contrary to the common notion that higher symmetry patterns have lower energies, in some cases, the CR or the FR alternatives have a lower global BNT energy. This is not surprising, as previous studies have shown that anticube (a CR version of the cube) patterns are more energetically favorable in certain tetratic systems [18–20].

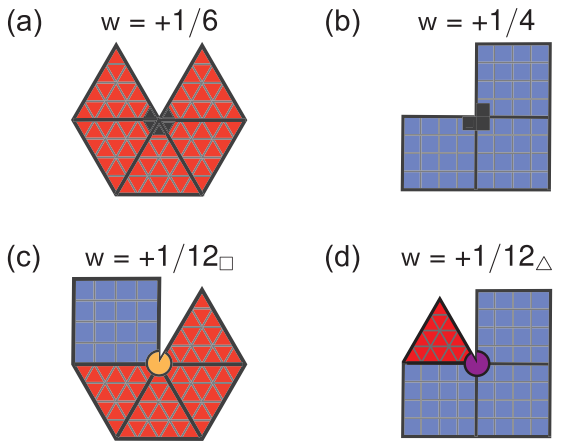

FIG. 1. Types of point defects examined in the current study on a spherical surface, where the flattened-out, cut views are presented. Plot (a) shows a winding number $w = +1/6$, produced by the closure of five triangular lattice domains. Plot (b) has $w = +1/4$, produced by the closure of three square lattice domains. Plot (c) is produced by inserting a square lattice domain into four triangular domains, resulting in a winding number $w = +1/12_{\square}$. Plot (d) can be viewed as the insertion of a triangular lattice domain into three square domains, with $w = +1/12_{\triangle}$. The subscripts $\square$ and $\triangle$ are used here to further distinguish the type of insertion. The color scheme of the illustrations, red for the triangular domain, blue square domain, orange defect point for $w = +1/12_{\square}$, and purple $w = +1/12_{\triangle}$, is preserved throughout the paper.

II. DEFECT PATTERNS WITH THE HIGHEST SYMMETRIES

In this section, possible defect patterns on a spherical surface tiled with triangular and square tiles are presented, after searching for all possible point-group symmetries of the global patterns. Symmetry always plays a critical role in determining the stability, organization, and physical properties of patterns on spherical surfaces, making it essential for understanding systems such as viral capsids, colloidal crystals, or geodesic domes [12].

On a spherical surface, the point disclination produced by arranging otherwise ideal lattices is characterized by the winding number w [38]. The basic types of low winding numbers considered in the current work are shown in Fig. 1, in triangular lattices [Fig. 1(a), $w = +1/6$], in square lattices [Fig. 1(b), $w = +1/4$], and in mixed triangular-square lattices [Figs. 1(c) and 1(d), $w = +1/12$]. Although other point disclinations are possible, including those with higher or negative w, the point disclinations in Fig. 1 are commonly believed to cause the least lattice deformations on a curved surface of positive Gaussian curvature [20], hence they are considered here.

According to the Euler-Poincaré theorem, the total, summed winding numbers of all disclinations on a closed curved surface must be the same as the Euler characteristic of the surface [2]. In the present case of a spherical surface for which the Euler characteristic is $+2$, there must be 12 $+1/6$ point disclinations when arranging triangular lattices, eight $+1/4$ point disclinations when arranging square lattices, and 24 $+1/12$ point disclinations when arranging

triangular-square lattices. The locations of these defect points on the spherical surface, together with the relative orientations of the lattice domains around these defect points, form a global defect structure, which can be identified by a point group. Some different patterns may share the same point-group operations.

Deformed tiles on a curved surface may not all have an identical shape. Caspar and Klug introduced the concept of quasi-equivalence, which requires the deformed tiles on a curved surface to have nearly identical shapes in order to maintain the overall stability and functionality of the entire structure. The structures on the spherical surface can be viewed as projections of the flat surfaces of a three-dimensional polyhedron, where the surfaces contain unstretched, identical tiles, on the spherical surface. Among the full list of polyhedra, those that follow the symmetries of Platonic solids, three-dimensional polyhedra with flat faces that are all the same regular polygons, are considered here, as they exhibit high space-group symmetries. These include full icosahedral (I_h), full octahedral (O_h), full tetrahedral (T_d), and N-dihedral (D_{Nh}) groups, as they contain the greatest number of symmetry operations. The corresponding polyhedra, including their truncated versions, are considered in our enumeration. Those that can be fitted with triangular and square tiles on their surfaces are identified and listed below in Secs. II A, II B, and II C.

A. Triangle tiles

The first example reviews the well-known symmetric defect patterns formed by triangular tiles. The icosahedral point-group symmetry is the highest symmetry that can be formed by 12 $w = +1/6$ defect points, located at the corner vertices of an ideal icosahedron (I_h). These vertices exhibit local fivefold symmetry around the defects and are represented in Figs. 2(a1) and 2(a2) by pentagonal defect points.

There are two different tiling patterns that accommodate low triangular lattice distortions over the entire spherical surface, icosahedron [first panel of Fig. 2(a1)] and dodecahedron [Fig. 2(a2)], each having their unique tile orientations with respect to the nearest defect-defect geodesic curves. This is more clearly observed in the polyhedron view, shown in the second panels of the plots. Along these curves, the edges of the triangles are consistently aligned to form a global structure in the icosahedron pattern. This alignment is easily understood by viewing the flattened-out icosahedron, before its projection onto the spherical surface [Fig. 2(a1), third panel]. In the dodecahedron pattern, on the other hand, the nearest defect-defect geodesic curves are always perpendicular to one of the edges of the triangles that fill the surface domains in between. This can again be visualized in the flattened-out view in Fig. 2(a2), third panel. Around the 12 $+1/6$ point defects, each pattern contains distorted triangular lattices that form 12 local pentagons, identical in shape. The relative orientations of the pentagons differ between the two patterns.

From symmetry alone, no conclusion can be drawn about which pattern, Fig. 2(a1) or Fig. 2(a2), has lower energy, since the two structures are identical from an elastic theory perspective [39]. Simulations [39,40] were conducted to compare the elastic energies of the two symmetries shown in Figs. 2(a1) and 2(a2). The simulation revealed a slight energy difference between the two states, with Fig. 2(a2) having the lower energy.

B. Square tiles

The point disclination with the lowest positive winding number is $+1/4$ for square lattices [Fig. 1(b)]. To tile the spherical surface with only $+1/4$ defect points, eight defect points must be distributed across the spherical surface. Following the same basic principles that lead to the defect patterns discussed in the previous section, the basic defect pattern is cubic, with full octahedral O_h point-group symmetry. The defect points, which have threefold local symmetry, are positioned at the corner vertices of a perfect cube [Figs. 2(b1) and 2(b2)].

The first cubic pattern is shown in Fig. 2(b1). Near the point-point line connecting two nearest defect points, the square tiles are diagonally arranged such that the two diagonal vertices align with the point-point line [see the polyhedron view in Fig. 2(b1)]. The second cubic pattern is shown in Fig. 2(b2). Near the line connecting the two nearest defect points, the edges of the square tiles are aligned parallel to the defect-defect line [see the polyhedron view in Fig. 2(b2)]. The difference between the two patterns can be easily identified in the flattened, cutout views in Figs. 2(b1) and 2(b2). Each of these two patterns has eight identical local defect regions, forming triangular defect domains. The simple-textured structure in Fig. 2(b2) has been suggested as the possible structure for the so-called "one-constant" systems [19].

C. Mixed triangle and square tiles

The main subject of this study is the mixed triangular-square tiling. Since the lowest possible positive defect point has a winding number of $+1/12$, 24 defect points are distributed over the spherical surface. In this case, there are four possible high-symmetry defect classes. All illustrations here contain triangles and squares of the same side lengths. When they have different side lengths, the lattice boundaries between the triangular and square domains may exhibit distortion to match the bond lengths. Here we assume that the distortion is localized to the boundaries, for which the boundaries in the illustrations are conceptual and should be viewed as narrow corridor regions.

The first class of patterns is the natural extension of the cubic patterns from the pure square tile case, where $f \lesssim 1$. The defect domains at the vertices of the cube already have a triangular shape [Figs. 2(b1) and 2(b2)]. Two defect patterns are possible, following the O_h point group.

With triangular tiles added, the pattern in Fig. 2(c1) is a truncated cube, where the triangular tiles fill the truncated triangular areas and the square tiles fill the cubic surface, with the square edges rotated by $\pi/4$ from the cube edges [see the first and second panels of Fig. 2(c1)]. The diamond pattern appears on the main cube faces.

The other pattern is a cantellated cube, shown in Fig. 2(c2). The cantellation operation can be understood as truncating the vertices of a regular polyhedron while simultaneously

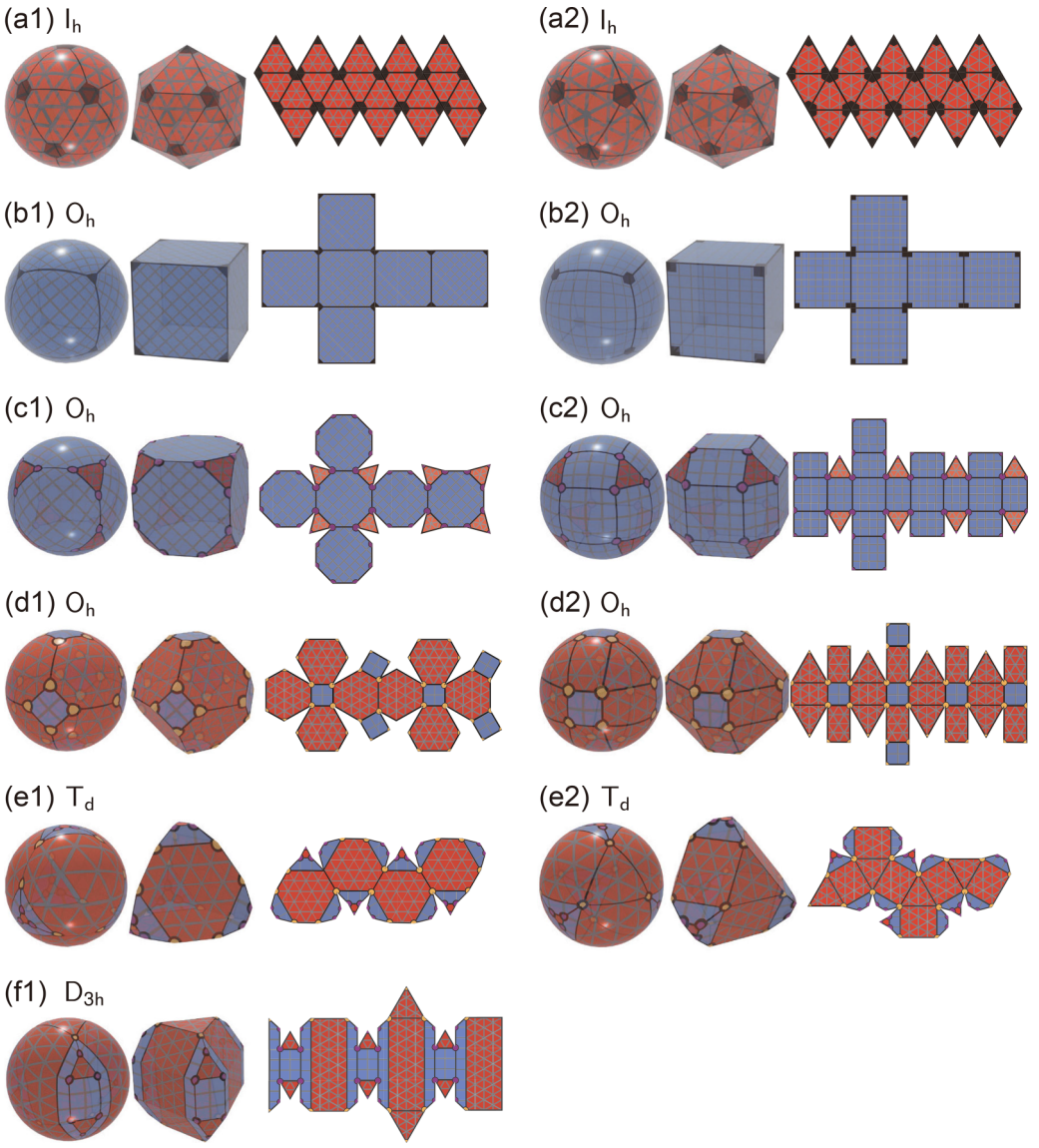

FIG. 2. Highest symmetries of defect patterns, determined for (a1)–(a2) triangular tiling [in [1]], (b1)–(b2) square tiling [(b2) suggested in [19]], and (c)–(f) mixed tiling. The first panels in these plots show 3D views of the patterns on the spherical surface, and the second panels display 3D views of the projected polyhedra, which further reveal the corresponding point-group symmetries. The third panels present flattened, cut views of the second panels. All triangular-tile domains are colored red, and all square-tile domains are colored blue. The polyhedra in (c1), (d1), and (e1) are a truncated cube, truncated octahedron, and truncated tetrahedron. The polyhedra in (c2), (d2), and (e2) are cantellated cube, cantellated octahedron, and cantellated tetrahedron. The solid lines on the spherical surfaces are not necessarily geodesics; they are included solely for illustrative purposes when projecting the polyhedron onto a spherical surface.

chamfering the edges, creating new faces at edges and vertices. The eight triangular domains still occupy the original cube corners but are rotated so that their edges align with the direction of the cube edges. The square lattices on the main cube surfaces form a pattern that matches the original cube edges. The 24 defect points, shown in the plot as orange circles, are located at the corners of the triangular areas. These points can be viewed as $w = +1/12_{\triangle}$ defects of the type shown in Fig. 1(c), corresponding to the insertion of triangles among the majority square tiles.

The second class of patterns, octahedral, also possesses O_h symmetry but is rich in triangular lattices, as shown in Figs. 2(d1) and 2(d2). When projected onto the polyhedron surfaces (second panels), these are truncated versions of originally regular octahedra. The corner-truncated version in Fig. 2(d1) contains six square domains at the corners of the octahedron, which are filled with square tiles. The main faces of the octahedron, shaped like triangular domains, are filled with triangular tiles. The other pattern, in Fig. 2(d2), is derived from Fig. 2(d1) by rotating all the square domains by a $\pi/4$ angle. This is best described as a cantellated octahedron, where the vertices and edges are orderly truncated. In this case, the square-domain edges are now all parallel in the cut-out view [third panels of Fig. 2(d2)]. In both cases, Figs. 2(d1) and 2(d2), the 24 defect points are located at the corners of the rectangular domains. These points can be viewed as $w = +1/12_{\square}$ defects, as shown in Fig. 1(d),

corresponding to the insertion of square tiles among the majority of triangular tiles.

The third class of patterns displays another major space-group symmetry, tetrahedral, T_d, shown in Figs. 2(e1) and 2(e2). The main faces of the original tetrahedron have a natural triangular shape (second panels), which accommodates the filling of triangular tiles. Square tiles begin to fill the truncated corners of the tetrahedron in both Figs. 2(e1) and 2(e2), which have a natural triangular domain shape. However, this arrangement is not sustainable near the domain center, where triangle domains filled by triangular tiles reoccur as insets. Two patterns of T_d are possible: truncated tetrahedron and cantellated tetrahedron, where the triangular domains at the corners of the original tetrahedron vertices have relatively different orientations, $\pi/3$ between Figs. 2(e1) and 2(e2). Because a square-tile domain only appears to enclose another triangular-tile domain, this structure can be stabilized at low f.

The fourth class is a truncated version of spherical hosohedron, shown in Fig. 2(f1), displaying the D_{3h} symmetry, where the threefold rotation axis is along north-south poles. In the truncated version, second panel of Fig. 2(f1), the north and south poles are located at the centers of the top and bottom triangular domains, where triangular tiles can be fitted. Three symmetric biangle regions, outlined by the blue square tile domains, start and end with a pair of $w = +1/12_{\square}$ defect points (hence a total of six defect points). The other 18 defect points of the type $w = +1/12_{\triangle}$ appear inside the three biangle regions and are located at the corners of two triangle domains of triangular tiles within each biangle region. This complex structure is expected to exist in the low-f range.

D. Gauss-Bonnet theorem

The above identification of defect patterns ensures the distribution of 24 defect points with a value of $w = +1/12$, obeying the Euler-Poincaré theorem [2]. The defect patterns in Figs. 2(c)–2(f) are in full compliance with another important mathematical theorem, the Gauss-Bonnet theorem, which dictates the relationships between the spherical area formed by geodesic curves of a domain and the allowed internal spherical angles when the geodesics of the domain intersect. A direct consequence is that the spherical triangle, for example, has a total internal angle $(1 + 4a)\pi$, where a is the area fraction of such a spherical-triangular domain compared to the entire surface.

Take the defect pattern in Fig. 2(c) as an example. When a is small, each of the eight triangular domains, located at the corners of the cube, has a total internal angle close to π and can be directly covered by triangular tiles. As a grows, however, the total internal angle becomes greater than π, and the triangular tiles experience more distortion to cover the area. An extreme case is $a = 1/8$; in this case, a typical internal angle of the spherical triangle is $\pi(1 + 4/8)/3 = \pi/2$; directly adjacent to such an angle, a square tile is a better fit. Hence, somewhere between $a \ll 1$ and $a = 1/8$, triangular tiling switches to square tiling. One can show that Fig. 2(c) switches to Fig. 2(d).

Take Fig. 2(d) as another example. A spherical square has a total internal angle $(1 + 2a)2\pi$. As $a \ll 1$, the internal angle is $\pi/2$, which is suited for square tiling. And at the maximum end, if the occupied area $a = 1/6$, such a spherical square has an internal angle $2\pi(1 + 2/6)/4 = 2\pi/3$, which is an angle that can be easily tiled by two triangles. Hence, as a grows, the pattern must switch over to triangular tiling. The transition must happen in between $a \ll 1$ and $a = 1/6$.

To conclude, depending on the area fraction of a spherical domain, the internal angles may be better suited to tilings with a specific type of symmetry, especially if minimal angular distortion is expected. The symmetries listed above allow for mutual switching.

An interesting case is the pattern in Figs. 2(e1) and 2(e2), based on tetrahedral symmetry. In a perfect tetrahedron with flat face, each of the four faces can be easily used to fit triangular tiles. However, when it is projected on the spherical surface, the interior angle of each would-be triangular domain becomes $2\pi/3$, which is a far stretch of the original $\pi/3$ angle from a triangular tiles, in a three-triangle formation. These corner regions, on the other hand, can be easily tiled by six triangles, as shown in the second panels of Figs. 2(e1) and 2(e2). For a small domain in these region, the simplest geometry is a triangle domain made of triangular lattices. Now, this tetrahedron structure has 12 $w = +1/6$ disclinations. To achieve the mixed triangular-square tilings, between the original tetrahedron faces and these corner triangle domains, stripes of square tiles fit. Take the blue, square-filled spherical triangles in Fig. 2(e) and increase their areas to $a = 1/8$ of the spherical surface. One can see that the interior angle is $\pi(1 + 4a)/3 = \pi/2$ following the Gauss-Bonnet theorem, which, of course, accommodates square tiles.

The pattern in Fig. 2(f1), following symmetry of D_{3h}, is a special case where the geometry exists only on the spherical surface. The total internal angle of the blue area is given by $4a\pi$ where a is the biangle area formed by two geodesic curves, according to the Gauss-Bonnet theorem. A perfect division into three biangle domains, from the north to south poles, makes the internal angle $2\pi/3$, which can be easily used for tiling six triangles near the polar region. If one reduces a, however, the internal angle becomes smaller. When a approaches $1/4$, the internal angle approaches $\pi/2$. Hence the enclosed domain can be tiled by squares (the blue region). Covering this domain by square tiles layer by layer from the biangle edges, one encounters a smaller biangle, when a approaches $1/6$. The internal angle now becomes $\pi/3$, on which triangular tiles are a much better fit. Hence, two triangular-shaped, triangle-tiled domains appear in each of the square-tiled biangle domains of Fig. 2(f1).

In cases Figs. 2(e) and 2(f), the Gauss-Bonnet theorem necessitates the formation of local enclave structures, as illustrated. It, however, does not produce the highly symmetric, global defect patterns.

E. Kaleidoscopic rotation

The enumeration produces symmetric structures in Secs. II A, II B, and II C, but alternative, less-symmetric structures with related symmetries can also be generated. These alternatives are described in this and the next subsections.

Within the same class of defect patterns, e.g., Figs. 2(a1) and 2(a2), the main difference is the orientations

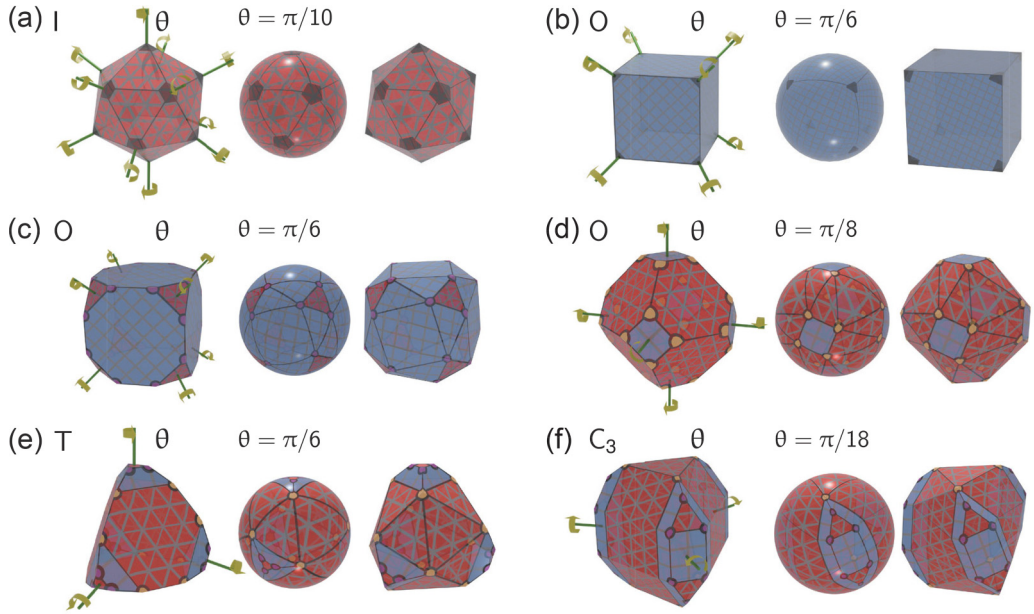

FIG. 3. Face rotations (kaleidoscopic rotations) of the patterns listed in the left panels of Figs. 2(a)–2(f). The rotation by an angle is performed simultaneously on the minor domains of each pattern, about axes that pass through the domain center and the spherical center. Such rotation maintains all tiling textures in the red and blue domains, relative to the domain boundaries. The rotational arrows illustrate a common counterclockwise FR angle θ. When $\theta = \pi/n$, where n represents the n-fold symmetry of the rotated domain, the patterns transform themselves into the patterns shown in the right panels of Fig. 2. Here $n = 5$ for the pentagonal disclination in (a), $n = 3$ for (b), (c), and (e);, and $n = 4$ for (d). For a general θ ($\theta \neq 0$ or π/n), the full symmetry is broken, specifically disrupting the inversion and reflective symmetries, leading to I, O, O, O, T, and C_3 symmetries, respectively. The corresponding spherical and polyhedral views of an FR pattern are shown in the second and third columns.

of the defect domains. They are related to each other by simultaneous rotation of such domains, at an angle θ, counterclockwise about the axis passing through the center of the defect and the spherical center. One can check that when the rotation occurs simultaneously, the boundaries of the bulk faces rotate to the same direction as well. Thus, the shape of the bulk is preserved and the lattice grains of the bulk domains are rotated but not disturbed. The rotational process can be more explicitly seen on a spherical surface, having some resemblance to generating patterns seen in a kaleidoscope, maintaining symmetries and repetitions of the same local patterns [41].

This method generates an entire set of new defect patterns, as suggested by Goldberg in 1937 [6], and Caspar and Klug in 1962 [1], to manipulate the original pattern into skewed icosahedral patterns in Fig. 3(a), as alternatives that can occur in triangular tiling. In the following we refer to this type of operation as the face-rotated (FR) alternative. We find here that the FR rotation can be performed on the patterns listed in Fig. 2 for square tilings and mixed triangle-and-square tilings.

The result is a set of skewed patterns, characterized by an angle θ. There are special cases. For example, when $\theta = \pi/5$ in Fig. 3(a), $\theta = \pi/3$ in Figs. 3(b) and 3(c), $\theta = \pi/4$ in Fig. 3(d), and $\theta = \pi/3$ in Fig. 3(e), starting from the patterns in Figs. 2(a1)–2(e1), the original space-group symmetries are recovered. The defect patterns are rotated to those in Figs. 2(a2)–2(e2), exactly. However, at an arbitrary FR angle θ between $\theta = 0$ and the specific values mentioned above, the system loses the highest symmetry of the original pattern; typically the inversion symmetry is destroyed. In our case, the kaleidoscope patterns in Figs 3(a)–3(f) have point-group symmetries I, O, O, O, T, and C_3 respectively, which can be compared with the original I_h, O_h, O_h, O_h, T_d, and D_{3h} in Fig. 2.

The FR operation for the hosohedral structure is limited due to the curved boundaries of the large truncated faces, as shown in Fig. 2(f1). When θ is small, adjacent lattice domains can still undergo rotation. However, at larger values of θ, such as $\theta = \pi/2$, three domains lie horizontally along a great circle. This configuration makes it impossible to tile the entire surface with a single triangular lattice, as the curvature prevents seamless tiling of the bulk area.

F. Cut-and-rotate patterns

The phrase cut-and-rotate (CR) was originally used to suggest a symmetry operation in a nematic liquid on a spherical surface [35,36]. The two +1 hedgehog point defects at the two opposite poles are cut by a great circle through the center, creating four +1/2 split defects. The entire pattern is then rotated by an angle about the common axis of the two hemispheres. In crystalline solids, a similar operation to generate related crystal structures, the mono-twinned operation, cuts along a plane followed by a rotational symmetry about the common axis [42].

Here we borrow the same concept to create new defect patterns for the spherical lattice system currently studied. As it turns out, CR states may have a lower energy than the original patterns, as discussed in the next section. The CR operation takes an existing rotational-symmetry axis of structures in

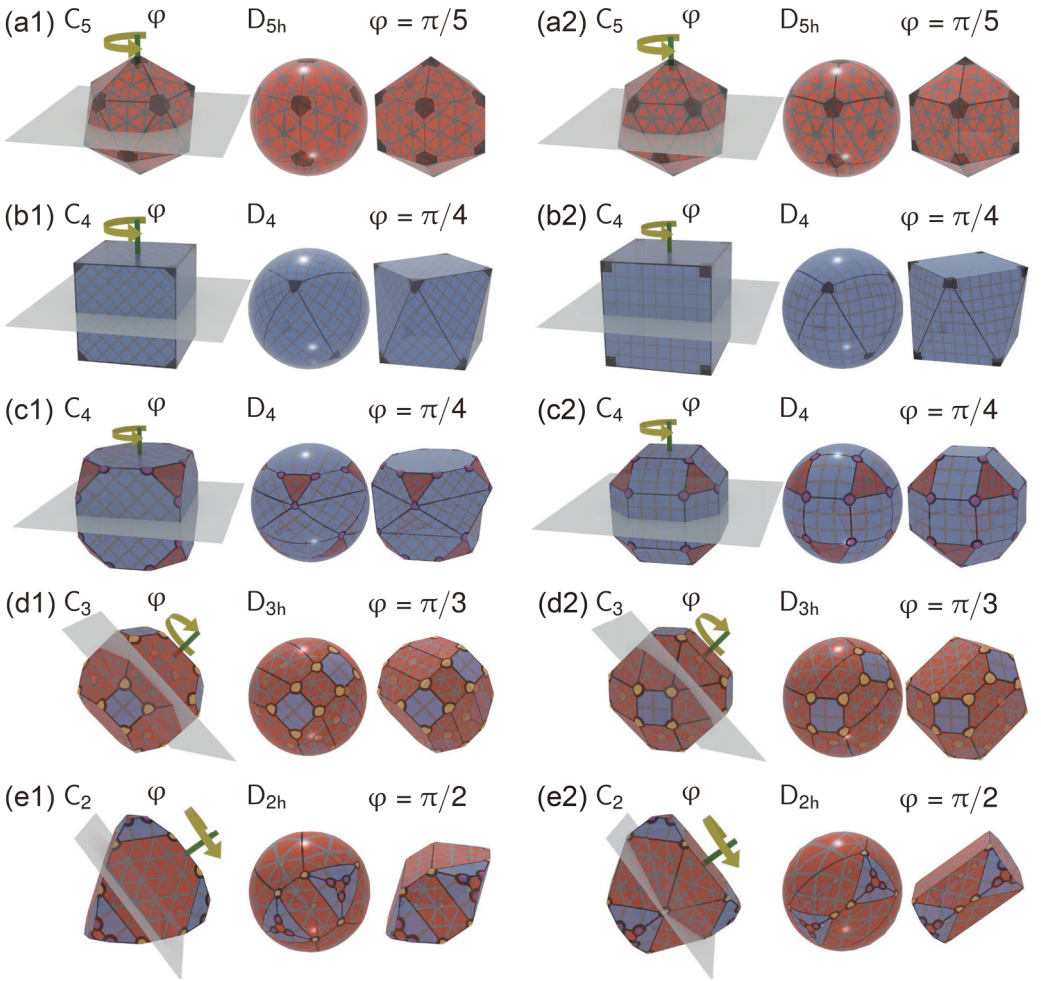

FIG. 4. Cut-and-rotate operations on the defect patterns listed previously. The translucent plane represents the equator plane where the polyhedron is cut into two halves. When projected onto a sphere, the lattice grain details at the cutting seam are identical after the CR operation. The angle φ describes counterclockwise rotation of the upper hemisphere about the spherical axis. For an arbitrary φ, the patterns in the first columns of the illustrations have space-group symmetries C_5, C_4, C_4, C_3, and C_2 for panels (a)–(e), respectively. When $\varphi = \pi/n$, where n corresponds to the n-fold symmetry of a hemisphere along the axis [i.e., $n = 5$ for (a), $n = 4$ for (b) and (c), $n = 3$ for (d), and $n = 2$ for (e)], a higher symmetry is achieved. Specifically, the structures in the second (3D view) and third (polyhedral view) columns of the illustrations have space groups D_{5h}, D_4, D_4, D_{3h}, and D_{2h} for (a)–(e), respectively.

Fig. 4 and cuts through the equatorial plane perpendicular to the axis provided that such a cut does not split an existing defect point. The upper hemisphere of the pattern is rotated by an angle φ counterclockwise about the rotational axis. A useful feature to consider is that, after the CR operation, the same gear-tooth-like configurations are recoverable, exactly matching the fine lattice grains on the two hemispheres at special values of φ. In theory, φ can only adopt discrete values to match this requirement; at the continuum limit, on the other hand, the lattices on both hemispheres along the cutting seam have the same fine configurations, and the rotation is smooth and continuous.

Given that the lattices here are made of triangular and square tiles, we discover that the CR operation can be performed on full symmetric patterns in Figs. 2(a)–2(e) and most of their FR counterparts in Figs. 3(a)–3(e) discussed above. The CR operations are illustrated in the first column of Fig. 4 together with the cutting planes. At an arbitrary CR angle φ, such a rotation destroys mirror symmetries of the original configuration, thereby producing a lower symmetry alternative. For example, the operations in Figs. 4(a)–4(e) yield symmetries C_5, C_4, C_4, C_3 and C_2 respectively, in comparison with the original I_h, O_h, O_h, O_h and T_d in Fig. 2. The hosohedral structure in Fig. 2(f1) does not have a valid cutting seam to conduct the CR operation.

There are special cases. When the angle $\varphi = \pi/n$ is used on a CR operation about a n-fold axis of the original patterns, a new symmetric pattern can be produced. The patterns shown in the second (3D view) and third (polyhedron view) columns of Figs. 4(a)–4(e) have the point-group symmetries D_{5h}, D_4, D_4, D_{3h} and D_{2h} respectively. Essentially, in comparison with those with an arbitrary φ, an original mirror symmetry is recovered, which results in the higher symmetries. In comparison with the original full symmetries, some of the rotational-symmetry operations are removed, hence the second and third columns of Fig. 4 have lower symmetries. Considering the phrase anticube is already used for the special case of a CR cube, shown in Fig. 4(b), the names anti-icosahedron [for

Fig. 4(a1)], antidodecahedron [for Fig. 4(a2)], antitruncated cube [for Fig. 4(c1)], anticantellated cube [for Fig. 4(c2)], antitruncated octahedron [for Fig. 4(d1)], anticantellated octahedron [for Fig. 4(d2)], antitruncated tetrahedron [for Fig. 4(e1)], and anticantellated tetrahedron [for Fig. 4(e2)], are given for the corresponding special structures.

Triangular tiling on a spherical surface has been extensively discussed in the literature. However, the CR version of the structures, in particular, anti-icosahedron and antidodecahedron, have not been commonly realized as possible alternatives to the original defect patterns. One example is the stable D_{5h} structure observed in C_{70} fullerene [7], which possesses 12 pentagons at the vertices of a pentaprism. Theoretically, it can be visualized as the CR of an angle $\varphi = \pi/5$ from the icosahedral symmetry of a C_{60} fullerene, though 10 additional particles need to be inserted in the equatorial plane.

As a final note, for square tilings, the special CR state with $\theta = \pi/3, \varphi = \pi/4$ [Fig. 4(b2)] has been suggested as the energetically preferred ground state, of liquid crystals confined on a spherical surface in Ref. [19] by a phenomenological theory. On the other hand, the special CR state with $\theta = 0, \varphi = \pi/4$ [Fig. 4(b1)] has been observed as the ground-state configuration in direct Monte Carlo simulations of tetratic molecules [18]. From a symmetry perspective, both states are possible high-symmetry anticube patterns.

G. Brief summary

So far, we have listed all possible high-symmetry tiling patterns for triangular, square, and mixed triangular-square lattices on spherical surfaces. Only low winding number point disclinations are considered in the symmetry analysis. Variations of the symmetric patterns, allowing face rotations of the defect regions and cut-and-rotate operations through an equatorial plane, are also introduced, which may lower the global defect symmetries.

The question remains as to which of the patterns is stable in actual physical systems, for a given area fraction f of the square lattice in the background of the triangular lattice (or vice versa) on the spherical surface. This requires the consideration of energetics at the molecular level or in continuum. As an example, the next section focuses on the effects of the BNT interaction between the defect points [12], which illustrates the possible low-energy patterns for a given f.

III. BNT ENERGY CURVES

A. BNT interaction

There are several levels of theoretical approaches that can be taken to study the defect patterns arising in a physical problem on a curved surface. At the molecular level, computer simulations can be performed based on a chosen molecule-molecule interaction [22,35,43–46]. Typically, a large number of molecules are placed in the system, which yields a final global pattern of the molecular positioning and orientation (if the molecules are anisotropically shaped). At a coarse-grained, field-based model, a vector or scalar density field, typically depending on the locations on the spherical surface, is designated as the order parameter; the system's energy is expressed in terms of the field and then minimized. Examples include the phenomenological descriptions of liquid-crystal patterns based on the Landau–de Gennes theory [47–50], Onsager model [51–53], Lebwohl-Lasher model [44,54], Rapini-Papoular model [55,56] as well as Oseen-Frank model [18,20,57–60].

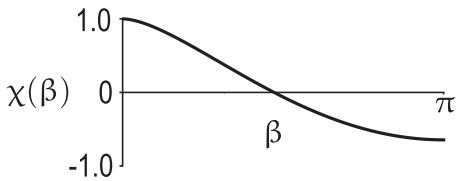

FIG. 5. The BNT interaction energy, $\chi(\beta)$ in Eq. (2) between two defect points, is displayed as a function of the geodesic angle β between them.

There is an even higher coarse-grained level, which emphasizes the stress on the distorted patterns on a curved surface, in comparison with their flat-space regular patterns, in the form of defect-defect interactions. At this level, the system energy is approximated by the interactions of isolated defect points, mediated by the microscopic molecular composition and surface density variation, which are not explicitly considered. In the ocean of background lattices formed by the actual molecules, the BNT potential energy, developed by Bowick, Nelson, and Travesset, provides a simple expression for the free energy that only depends on the types and positions of the defects [37,39]. In liquid-crystal theory, such an approach is also possible [61].

Here we use the BNT interaction as a general framework for the global elastic energy of the entire pattern. In comparison with the background energy in a flattened space, the key BNT energy is

$$\Delta E = \frac{1}{2}\sum_{i=1}^{N}\sum_{j=1}^{N} K_{ij}\chi(\beta_{ij}) + \sum_{j=1}^{N}\epsilon(w_j), \tag{1}$$

where w_i is the winding number of the ith disclination, K_{ij} is the reduced stretching modulus between defect points i and j, and $\epsilon(w_j)$ is the core energy of an isolated defect. In our notation, a $w_i w_j$ factor in the first term has been absorbed into the reduced K_{ij}. The interaction energy is written in terms of the geodesic angle β_{ij} between the ith and jth defect points, such that

$$\chi(\beta) = 1 + \int_0^{(1-\cos\beta)/2} dz \frac{\ln(z)}{1-z}. \tag{2}$$

One can show that it is repulsive (see Fig. 5).

B. Energy curves

For the current problem, there are $N = 24$ defects of types $w = +1/12_{\square}$ or $w = +1/12_{\triangle}$. For simplicity, in this subsection, a one-K approximation, $K_{ij} = K$ is taken, and the last sum is dropped assuming two types of $+1/12$ defects have the same effects. In all cases considered below, an area fraction f is used to represent the area fraction of the square lattice regions on the curved surface, composed of geodesic boundaries.

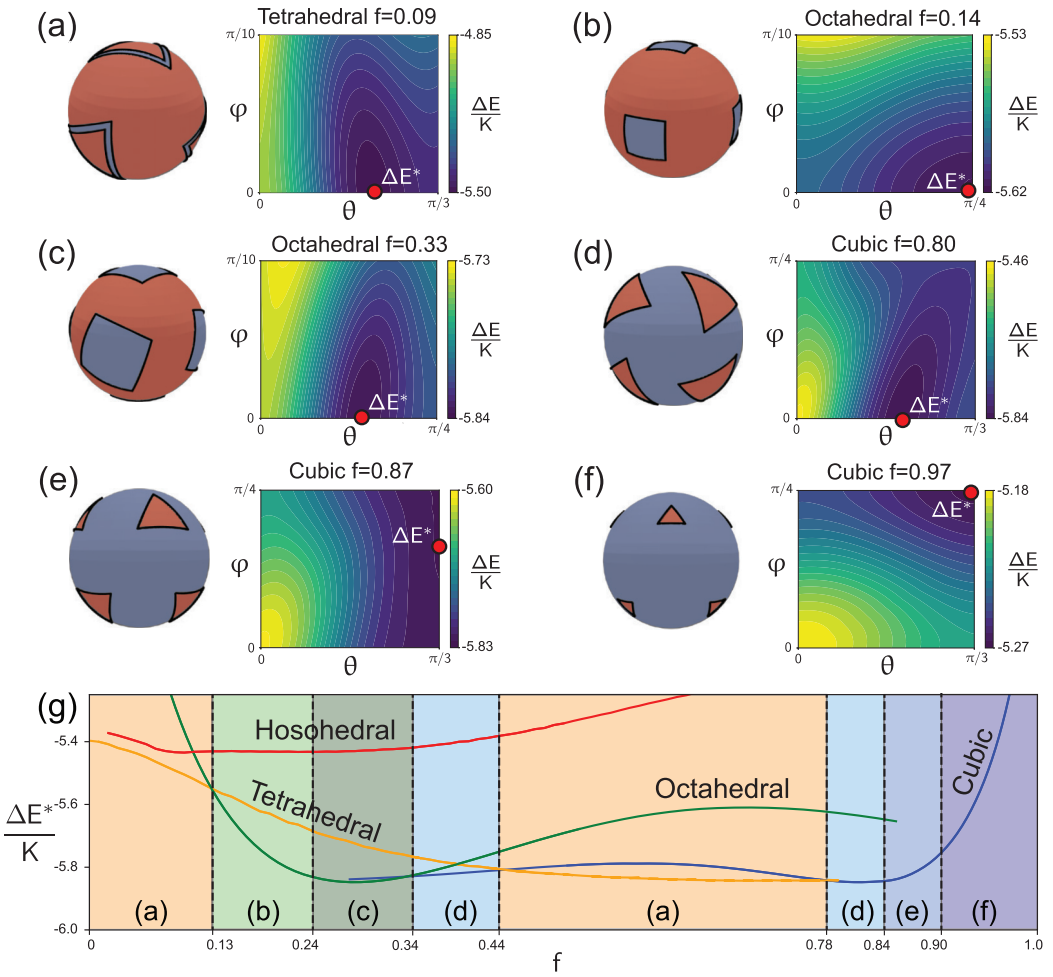

FIG. 6. BNT energy of all studied defect patterns for a given f. Typical defect domains that exhibit the lowest BNT energy minima are illustrated below. (a) Tetrahedral pattern at $f = 0.09$, ΔE^* at $(\theta, \phi) = (2\pi/9, 0)$. (b) Octahedral pattern at $f = 0.14$, ΔE^* at $(\pi/4, 0)$. (c) Octahedral pattern at $f = 0.33$, ΔE^* at $(3\pi/16, 0)$. (d) Cubic pattern at $f = 0.80$, ΔE^* at $(2\pi/9, 0)$. (e) Cubic pattern at $f = 0.87$, ΔE^* at $(\pi/3, \pi/6)$. (f) Cubic configuration at $f = 0.97$, ΔE^* at $(\pi/3, \pi/4)$. In each plot the energy surface $\Delta E(\theta, \varphi)$, as a function of the FR angle θ (see Sec. II E) and CR angle φ (see Sec. II F), is also displayed, where the location of the energy minimum is indicated by a red circle. Plot (g) summarizes our findings for a given f, showing the different symmetry branches: cubic (blue), tetrahedral (orange), octahedral (green), and hosohedral (red). Vertical dashed lines mark the boundaries where the energy minimum transits from one branch to another.

For each class, the total BNT energy is calculated according to (1) with fixed values of f, θ, and ϕ, when all geometric features are fixed. As the first example for small f within $f = [0, 0.13]$, the energy minimum ΔE^* of the tetrahedral pattern is located at $\varphi = 0$ and a nontrivial value of θ, shown in Fig. 6(a). The FR pattern T is the most stable. This can be physically understood by the illustration in the left panel in Fig. 6(a). For small-f, the square lattices only occupy the narrow edges of the truncated domains; however, the affected defect domains can be significantly large. The large square lattice domains (blue color) require the rotation of the defect regions, to avoid the direct collision of the blue regions. The calculated ΔE^* is displayed in Fig. 6(g), where region (a) highlights the stability of T.

As f increases further, within $f = [0.13, 0.34]$, the octahedral patterns have a lower BNT energy than T, taking over the energy branch of the T pattern. The energy plot in Fig. 6(b) shows that the octahedron O_h pattern in Fig. 2(d2) has the energy minimum in $f = [0.13, 0.24]$, where $\theta = \pi/4$ and $\varphi = 0$. In the relatively larger $f = [0.24, 0.34]$ region, the blue square domains in Fig. 6(c) begin to interact more significantly and the face-rotated version, O shown in the left panel of Fig. 6(c), has a lower energy minimum. These two regions, (b) and (c), are represented in Fig. 6(g) by the light and dark green shades.

In the middle f region, $f = [0.34, 0.44]$, the FR cubic pattern, which has the symmetry O, has a lower energy minimum. The energy plot is shown in Fig. 6(d), indicating a nontrivial θ value, an FR alternative of Fig. 2(c2). In this middle-f region, the defect points are evenly spread out on the spherical surface. The configurational differences of the spreading, of the tetrahedral pattern in Fig. 6(a), the octahedral in Fig. 6(c), and cubic in Fig. 6(d), give rise to minor energy-minimum

differences, where the three energy branches in Fig. 6(g) are closely spaced.

In the mid-high region, $f = [0.44, 0.78]$, the close energy difference between T pattern in Fig. 6(a) and O in Fig. 6(d) remains. The patterns in Fig. 6(a) reenter as the most stable pattern. The evenness of defect spreading on the surface can also be observed in both cases.

Coming from the high-f side, $f = [0.78, 1]$, the cubic patterns are most stable. Near $f = 1$, the pattern corresponding to a lower space-group symmetry D_4 has a lower energy, where $\theta = \pi/3$ and $\phi = \pi/4$. The pattern is a CR alternative of the pattern in Fig. 2(c2), i.e., Fig. 4(c2). The energy plot on the right panel of Fig. 6(f) indicates that the patterns in Figs. 2(c1) and 2(c2) are not even metastable; one is actually an energy maximum and the other saddle point.

Across $f = 0.90$ from the high-f region, the perfect CR alternative loses its D_4 symmetry, as φ is lowered from the ideal $\pi/4$ value. A general CR alternative is observed. As $f = 0.84$ is approached from the high-f side, φ starts to approach another ideal value, $\varphi = 0$. The cubic pattern in Fig. 2(c2) is realized at a single value of $f = 0.84$, where its saddle-point energy becomes a true minimum.

Below $f = 0.84$, an FR alternative of the pattern illustrated in Fig. 6(d) appears as the energy minimum. Starting from the ideal pattern, the defect regions in Fig. 2(c2), begin to face rotate, towards the pattern in Fig. 2(c1) as the would-be target. The cubic energy minimum branch is the lowest among other possibilities in the region $f = [0.78, 0.84]$.

C. Brief summary

Figure 6(g) presents all BNT energies of the patterns described above. A few remarks can be made about the general features. (1) The hosohedral pattern indeed shows an energy minimum at $\theta \approx \pi/18$ and $f = 0.09$, but that branch, represented by the red curve in the plot, is always higher than the others. Thus, the hosohedral patterns are only metastable. (2) All energy minimum curves correspond to either an FR or CR alternative, but never both. There is only one energy minimum on the two-dimensional $\Delta E(\theta, \varphi)$ plots, hence only a single stable (or metastable) pattern for a given f within a given class of patterns. (3) The results have been presented as a function of simultaneous face rotation of all defect regions of a given ideal pattern, at a common angle θ. We have also tested another possibility, namely, allowing all defect regions to rotate independently of each other using a minimization calculation, while keeping the centers of the defect regions fixed on the surface. The process all converges back to the same θ rotation. Thus, the physical picture of simultaneous face rotation is justified. (4) The systems with larger square domains tend to form the FR patterns. To avoid the closing of repulsive defect points, a rotated pattern spreads out the distance between the defects more evenly.

IV. SUMMARY AND DISCUSSION

Based on a symmetry analysis, we studied the global symmetries of the defect patterns that can form when the spherical surface is tiled by a mix of triangular and square tiles. Four basic pattern classes are found: cubic, octahedron, tetrahedron, and trihosohedron, with symmetries O_h, O_h, T_d, and D_{3h}, respectively.

These patterns are clearly presented in the polyhedron views, in which the triangular and square tiles fill the available flat surfaces of the truncated and cantellated polyhedra with no distortion, as required by the quasi-equivalence concept of tiling the surface. Within each class, two different patterns are possible depending on the orientation of the filling tiles. Alternatives to these patterns, known as kaleidoscopic and cut-and-rotate patterns, are also proposed for these classes.

When projected onto the spherical surface, each flat surface in the polyhedron views becomes curved and experiences shape deformation. In the second part of the paper, we explore the possible consequences of this deformation in terms of the BNT energy. For a given area fraction of square tiles, only one of all the possible patterns (the original and alternatives) in a class reaches an energy minimum. By comparing the minima across the four classes, we suggest a preferred type of tiling pattern for specific ranges of f.

There are several complications that may impact the final results. (1) One such complication is the finite-size effect, which already exists in the triangular-tiling problem. In a finite system, given the area of the spherical surface, there is a relationship between the total number of tiles (the magic number) and an optimal symmetry pattern. Adding another tile is likely to alter or even destroy the entire symmetry. We essentially take a continuum limit, assuming many small tiles fill the available space and that magic numbers can be naturally established for a large system. (2) Another issue unique to tiling a surface with mixed triangular-square tiles is the line tension problem between the triangular and square lattice domains. The basic components of the system are individual, premade triangular and square tiles. The potential mismatch in tile side lengths requires lattice distortion along the boundaries between the triangular and square lattice domains. This can significantly affect the second part of the study, as the energy produced by line tension should be incorporated into the theory. The line tension introduces an additional parameter, calling for another dimension in the state diagram presented in Fig. 6, which is not considered here. (3) Instead of premade tiles, many surface structures in real systems are self-assembled from isotropic molecules. The triangular and square lattices result from self-assembly, not from a rigid structure to begin with. The coexistence of these lattices is closely related to a first-order phase transition between triangular and square crystal orderings. In this case, f should be treated as an adjustable parameter, along with the number density of the molecules, in a complete free-energy consideration. (4) In this study, we used a one-elastic-constant approximation. The difference in elastic energies (notionally represented by the the K_{ij} tensor in a coarse-grained consideration) as well as the difference in the two different types of $1/12$ defects [i.e., the ϵ term in Eq. (1)] can significantly affect the outcome of the energy analysis. (5) The use of the BNT interaction in an isotropic form, as given by Eq. (2), ignores the relative orientations of the defect points and their grain texture directions in between. This is already an issue, even for triangular tiling. Remedying this effect, which involves mixed media made up of triangular and square tiles, requires further research.

These complications impact the energy landscape of the problem. While the symmetry analysis in Sec. II likely remains the same, the energy analysis in Sec. III could be significantly altered. We hope that the current energy study captures some essential features of mixed tilings.

ACKNOWLEDGMENTS

The authors acknowledge the financial support from National Natural Science Foundation of China (12275137) and Natural Sciences and Engineering Council of Canada (NSERC).

[1] D. L. D. Caspar and A. Klug, Cold Spring Harb. Symp. Quant. Biol. **27**, 1 (1962).
[2] H. Poincaré, *Analysis situs* (Gauthier-Villars, Paris, 1895).
[3] A. Klug, Annu. Rev. Biochem. **79**, 1 (2010).
[4] F. H. Crick and J. D. Watson, in *Ciba Foundation Symposium-Steroid Hormones and Enzymes (Book II of Colloquia on Endocrinology)* (John Wiley & Sons, Ltd., Chichester, 1957), pp. 5–18.
[5] G. J. Morgan, Trends Biochem. Sci. **28**, 86 (2003).
[6] M. Goldberg, Tohoku Math. J. **43**, 104 (1937).
[7] H. W. Kroto, J. R. Heath, S. C. O'Brien, R. F. Curl, and R. E. Smalley, Nature (London) **318**, 162 (1985).
[8] W. H. Roos, R. Bruinsma, and G. J. L. Wuite, Nat. Phys. **6**, 733 (2010).
[9] J. E. Johnson and A. J. Olson, J. Biol. Chem. **296**, 100554 (2021).
[10] J. M. Fletcher, R. L. Harniman, F. R. H. Barnes, A. L. Boyle, A. Collins, J. Mantell, T. H. Sharp, M. Antognozzi, P. J. Booth, N. Linden *et al.*, Science **340**, 595 (2013).
[11] J. B. Bale, S. Gonen, Y. Liu, W. Sheffler, D. Ellis, C. Thomas, D. Cascio, T. O. Yeates, T. Gonen, N. P. King, and D. Baker, Science **353**, 389 (2016).
[12] M. J. Bowick and L. Giomi, Adv. Phys. **58**, 449 (2009).
[13] Y. Liu, H. Lei, Q.-Y. Guo, X. Liu, X. Li, Y. Wu, W. Li, W. Zhang, G. Liu, X.-Y. Yan *et al.*, Chin. J. Polym. Sci. **41**, 607 (2023).
[14] D. R. Nelson, *Defects and Geometry in Condensed Matter Physics* (Cambridge University Press, Cambridge, 2002).
[15] J. Echeverría, D. Casanova, M. Llunell, P. Alemany, and S. Alvarez, Chem. Commun. **24**, 2717 (2008).
[16] Y.-T. Lai, E. Reading, G. L. Hura, K.-L. Tsai, A. Laganowsky, F. J. Asturias, J. A. Tainer, C. V. Robinson, and T. O. Yeates, Nat. Chem. **6**, 1065 (2014).
[17] M. Pang, A. J. Cairns, Y. Liu, Y. Belmabkhout, H. C. Zeng, and M. Eddaoudi, J. Am. Chem. Soc. **135**, 10234 (2013).
[18] Y. Li, H. Miao, H. Ma, and J. Z. Y. Chen, Soft Matter **9**, 11461 (2013).
[19] O. V. Manyuhina and M. J. Bowick, Phys. Rev. Lett. **114**, 117801 (2015).
[20] T. C. Lubensky and J. Prost, J. Phys. II **2**, 371 (1992).
[21] T. Chen, Z. Zhang, and S. C. Glotzer, Langmuir **23**, 6598 (2007).
[22] W. L. Miller and A. Cacciuto, Soft Matter **7**, 7552 (2011).
[23] N. P. King, J. B. Bale, W. Sheffler, D. E. McNamara, S. Gonen, T. Gonen, T. O. Yeates, and D. Baker, Nature (London) **510**, 103 (2014).
[24] M. Mosayebi, D. K. Shoemark, J. M. Fletcher, R. B. Sessions, N. Linden, D. N. Woolfson, and T. B. Liverpool, Proc. Natl. Acad. Sci. USA **114**, 9014 (2017).
[25] A. Khmelinskaia, A. Wargacki, and N. P. King, Curr. Opin. Microbiol. **61**, 51 (2021).
[26] K. Zhao, R. Bruinsma, and T. G. Mason, Proc. Natl. Acad. Sci. USA **108**, 2684 (2011).
[27] L. Rossi, V. Soni, D. J. Ashton, D. J. Pine, A. P. Philipse, P. M. Chaikin, M. Dijkstra, S. Sacanna, and W. T. M. Irvine, Proc. Natl. Acad. Sci. USA **112**, 5286 (2015).
[28] B. Li, D. Zhou, and Y. Han, Nat. Rev. Mater. **1**, 15011 (2016).
[29] M. Rey, A. D. Law, D. M. A. Buzza, and N. Vogel, J. Am. Chem. Soc. **139**, 17464 (2017).
[30] S. Singh, P. Bandyopadhyay, K. Kumar, and A. Sen, Phys. Rev. Lett. **129**, 115003 (2022).
[31] M. Zu, J. Liu, H. Tong, and N. Xu, Phys. Rev. Lett. **117**, 085702 (2016).
[32] Z. Yao, Phys. Rev. E **101**, 062904 (2020).
[33] S. Paquay, H. Kusumaatmaja, D. J. Wales, R. Zandi, and P. van der Schoot, Soft Matter **12**, 5708 (2016).
[34] H. Xie, W. Liu, Z. Lu, J. Z. Y. Chen, and Y. Li, Nano Lett. **25**, 1193 (2025).
[35] H. Shin, M. J. Bowick, and X. Xing, Phys. Rev. Lett. **101**, 037802 (2008).
[36] X. Xing, H. Shin, M. J. Bowick, Z. Yao, L. Jia, and M.-H. Li, Proc. Natl. Acad. Sci. USA **109**, 5202 (2012).
[37] M. J. Bowick, D. R. Nelson, and A. Travesset, Phys. Rev. B **62**, 8738 (2000).
[38] P. M. Chaikin and T. C. Lubensky, *Principles of Condensed Matter Physics* (Cambridge University Press, Cambridge, 1995).
[39] M. J. Bowick, A. Cacciuto, D. R. Nelson, and A. Travesset, Phys. Rev. B **73**, 024115 (2006).
[40] E. L. Altschuler, T. J. Williams, E. R. Ratner, R. Tipton, R. Stong, F. Dowla, and F. Wooten, Phys. Rev. Lett. **78**, 2681 (1997).
[41] C. Adams, C. Edgar, P. Hollander, and L. Jacoby, Discrete Comput. Geom. **72**, 1029 (2024).
[42] B. Raoult, J. Farges, M. F. De Feraudy, and G. Torchet, Philos. Mag. B **60**, 881 (1989).
[43] M. A. Bates, J. Chem. Phys. **128**, 104707 (2008).
[44] G. Skačej and C. Zannoni, Phys. Rev. Lett. **100**, 197802 (2008).
[45] S. Dhakal, F. J. Solis, and M. Olvera de la Cruz, Phys. Rev. E **86**, 011709 (2012).
[46] J. M. Ilnytskyi, A. Trokhymchuk, and M. Schoen, J. Chem. Phys. **141**, 114903 (2014).
[47] P.-G. De Gennes and J. Prost, *The Physics of Liquid Crystals* (Oxford University Press, Oxford, 1993).
[48] M. Huber and H. Stark, Europhys. Lett. **69**, 135 (2004).
[49] P. Biscari, M. C. Calderer, and E. M. Terentjev, Phys. Rev. E **75**, 051707 (2007).
[50] M. Ravnik and S. Žumer, Liq. Cryst. **36**, 1201 (2009).
[51] L. Onsager, Ann. N.Y. Acad. Sci. **51**, 627 (1949).
[52] W.-Y. Zhang, Y. Jiang, and J. Z. Y. Chen, Phys. Rev. Lett. **108**, 057801 (2012).
[53] Q. Liang, S. Ye, P. Zhang, and J. Z. Y. Chen, J. Chem. Phys. **141**, 244901 (2014).

[54] P. A. Lebwohl and G. Lasher, Phys. Rev. A **6**, 426 (1972).
[55] A. Rapini and M. Papoular, J. Phys. Colloq. **30**, C4 (1969).
[56] B. I. Lev, S. B. Chernyshuk, P. M. Tomchuk, and H. Yokoyama, Phys. Rev. E **65**, 021709 (2002).
[57] F. C. Frank, Discuss. Faraday Soc. **25**, 19 (1958).
[58] D. R. Nelson, Nano Lett. **2**, 1125 (2002).
[59] W.-Y. Zhang, Y. Jiang, and J. Z. Y. Chen, Phys. Rev. E **85**, 061710 (2012).
[60] J. V. Selinger, Liq. Cryst. Rev. **6**, 129 (2018).
[61] V. Vitelli and D. R. Nelson, Phys. Rev. E **74**, 021711 (2006).